INORGANIC CHEMISTRY
FRONTIERS

RESEARCH ARTICLE

View Article Online
View Journal | View Issue

Cite this: *Inorg. Chem. Front.*, 2024, **11**, 1828

Synthetic ease and exceptional *in vivo* performance of pyrazole-based cyclometallated iridium complexes†

Marta Redrado, [a] Eduardo Romanos,[b] Andrea Benedi, [c] Guillermo Canudo-Barreras,[a] Isabel Marzo,[c] M. Concepción Gimeno *[a] and Vanesa Fernández-Moreira *[a]

Two luminescent cyclometallated Ir^{III} complexes of the type $[Ir(C^N)_2(N^N)]^x$ (X = 0 (**1**), and X = +1 (**2**)) were prepared using methyl 2-phenylquinoline-4-carboxylate as C^N ligands and either a deprotonated or protonated 3-(2-pyridyl)pyrazole as the N^N chelate. The synthesis followed a well-established and straightforward procedure. Photophysical analysis unveiled their remarkable properties, featuring phosphorescent red and orange emissions attributed to ^{3}MLCT and ^{3}LLCT transitions, with high emissive quantum yields in degassed DMSO solutions. Importantly, these complexes exhibited dual functionality as potent chemotherapeutic agents and photosensitisers, with their effectiveness tailored to specific cancer cell lines. Phototherapeutic treatment was particularly effective against lung cancer A549 cells, while a chemotherapeutic approach yielded superior results against breast cancer 4T1-luc2 cells. Both complexes primarily targeted lysosomes, leading to cell death through apoptotic pathways, with IC_{50} values in the nanomolar range. Importantly, they demonstrated no cytotoxicity against lymphocytes, mimicking the behaviour observed in healthy cells. Encouragingly, **1** and **2** exhibited minimal *in vivo* toxicity. The most striking finding was the exceptional chemotherapeutic efficacy of complexes **1** and **2** against 4T1-luc2 cells in BALB/c mice. These complexes surpassed the performance of the clinically employed 5-fluorouracil, especially at early tumor stages, significantly retarding 4T1-luc2 proliferation. Further investigations at vascularised and organised tumor stages revealed that complex **1** could reduce tumor size by half compared to untreated mice, which was also confirmed through tumoral weight analysis. While these findings are preliminary, the outstanding performance of these complexes at early tumor stages against breast cancer 4T1-luc2 *in vivo*, their selective therapeutic feasibility (chemotherapy *vs.* PDT) tailored to specific cancerous cell lines, and their straightforward synthetic design make them highly attractive candidates for cancer treatment.

Received 13th November 2023,
Accepted 2nd February 2024

DOI: 10.1039/d3qi02355a

rsc.li/frontiers-inorganic

Introduction

Cyclometallated iridium complexes have emerged as promising alternatives to platinum-based anticancer drugs in chemotherapy.[1] In addition, they have been reported to function as efficient photosensitisers (PSs) producing reactive oxygen species (ROS), such as the highly cytotoxic singlet oxygen ($^1O_2$).[2] This has opened the door to including cyclometallated Ir^{III} complexes within photodynamic therapy, potentially creating multifunctional therapeutic metallodrugs capable of serving as both chemotherapeutics and PSs agents. Additionally, their phosphorescent nature with high quantum yield, large Stokes shifts and long-lived phosphorescence, among other features, makes them also suitable for bioimaging.[3] One of the advantages of cyclometallated iridium complexes of the type $[Ir(C^N)_2(N^N)]^{+/0}$ is the possibility of incorporating pharmacophoric motifs in the form of ligands, broadening the scope of their applications in therapy. The easy modification of these ligands leads to a feasible modulation of the biological and photophysical properties for the cyclometallated iridium complex.[4]

The pyrazole motif is a significant component of heterocycles and is commonly present as a key element in numerous

[a]*Departamento de Química Inorgánica, Instituto de Síntesis Química y Catálisis Homogénea (ISQCH) CSIC-Universidad de Zaragoza, 50009 Zaragoza, Spain. E-mail: vanesa@unizar.es, gimeno@unizar.es*
[b]*Departamento de Imagen y Fenotipado, Instituto Aragonés de Ciencias de la Salud. Centro de Investigación Biomédica de Aragón (CIBA), 50009 Zaragoza, Spain*
[c]*Departamento de Bioquímica y Biología Celular, Universidad de Zaragoza, 50009 Zaragoza, Spain*

† Electronic supplementary information (ESI) available. See DOI: https://doi.org/10.1039/d3qi02355a

commercially available drugs.[5] Examples of the pyrazole-based commercial drugs include Tartrazine and Pyrazofurin (anticancer),[6] Deracoxib, Lonazolac, Celecoxib, Tepoxalin, and Ramifenazone (nonsteroidal anti-inflammatory drugs, NSAIDs),[7] as well as Difenamizole and Metamizole (analgesic) (see Fig. 1).[8] Hence, the pyrazole motif has been incorporated as a component of cyclometallated ligands (C^N), forming complexes with remarkably potent anticancer capabilities,[9] as well as in the diimine derivate (N^N) rendering theragnostic agents[10] (Fig. 1, examples A–D). Despite the great possibilities of the pyrazole motif, its utilisation is not as widespread in the realm of anticancer complexes. Instead, its primary applicability when combined with cyclometallated iridium species lies in the optical field and catalysis.[11]

On the other hand, lysosomes are involved in various aspects of cell death. Moreover, in cancer cells, lysosomes are more numerous and larger, making them very attractive targets for an anticancer drug.[12] Their acidic microenvironment (pH 4.5–5) results very favourable to trap molecules containing protonable groups such as amines. Several cyclometallated iridium complexes containing amines in their ligand design have been demonstrated to be selective probes for lysosomes.[13]

Our approach focuses on the development of two critical aspects: firstly, the design of synthetically straightforward lysosome-targeted cyclometallated iridium complexes; secondly, their utility as versatile chemotherapeutic and photosensitising agents. To achieve this, pyrazole was incorporated within the diimine ligand's design (N^N). This inclusion not only enables lysosome targeting through its amine group but also enhances water solubility and improves cellular uptake. Because the activation of a PS needs to occur at low energies to improve light penetration and ensure efficient photodynamic therapy, the selection of cyclometallated ligands (C^N) was a crucial aspect. C^N ligands are known to play a pivotal role in determining the photophysical properties of the final prototype, therefore, a highly aromatic platform was used to extend the optical properties towards the NIR region (see Fig. 2A). Furthermore, additional functionalisation was carried out to enhance cellular permeability while ensuring the ease of synthesis for the final metallodrug.

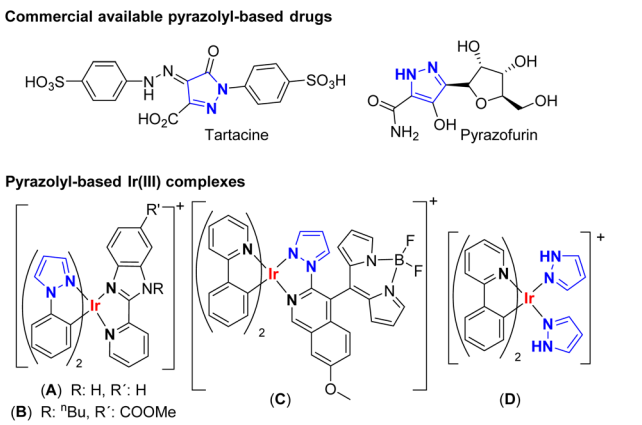

Fig. 1 Chemical structures of commercial available anticancer drugs containing a pyrazole motif and some examples of pyrazol based Ir^{III} complexes.

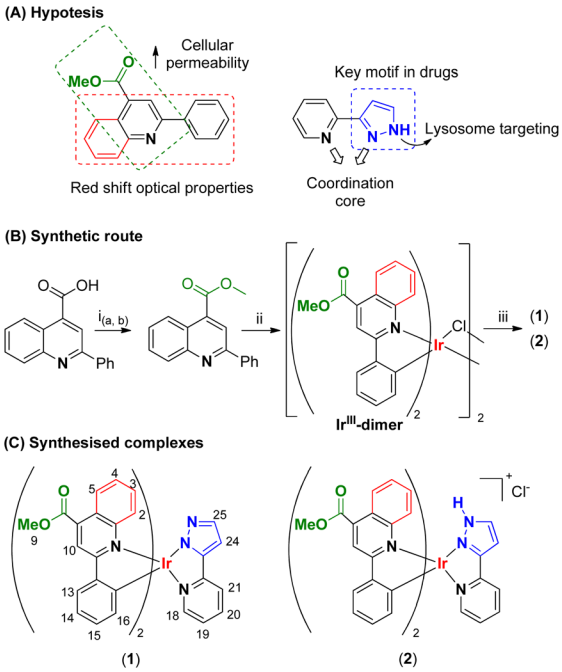

Fig. 2 (A) Hypothesis-based approach to probe design. (B) Synthetic pathway to prepare **1** and **2**. (i_a) $SOCl_2$, MeOH, (0 °C); (i_b) reflux, 2 h; (ii) $IrCl_3{\cdot}nH_2O$, 2-etoxyethanol, reflux, 24 h; (iii, **1**) 3-(2-pyridyl)pyrazole, Cs_2CO_3, DCM, 318 K, 20 h; (iii, **2**) DCM : MeOH (1 : 1), 298 K, 24 h. (C). Synthesised cyclometallated Ir^{III} complexes.

Results and discussion

Design and synthesis of complexes 1 and 2

To obtain the desired iridium-based PS agents, the first step was to select a suitable C^N ligand that, once incorporated to the metal centre can deliver soluble and photostable complexes in biological media, capable of being activated by low energy irradiation for the treatment of inner tumors. Therefore, it was envisaged that phenylquinoline-4-carboxylic acid as C^N ligand could fulfil such features. This molecule has extended aromaticity and less flexibility than analogous 2-phenylpyridine (ppy), which is expected to deliver a red-shifted optical properties. Moreover, its carboxylic group allows for easy functionalisation, opening the scope of introducing a great variety of functionalities, Fig. 2(A). Therefore, the carboxylate group underwent conversion into a methyl ester following a synthetic pathway previously outlined by DasGupta and coworkers.[14] This transformation yielded methyl-2-phenylquinoline-4-carboxylate (mpc), which will assist to enhance cell permeation in biological media. Subsequently, the cyclometallated precursor, $[Ir(mpc)_2(\mu\text{-}Cl)]_2$, was prepared according to an adaptation to conventional procedures, by reaction of

$IrCl_3{\cdot}6H_2O$ with mpc in ethoxyethanol instead of a mixtures of ethoxyethanol : water[15] (see Fig. 2(B)). Afterwards, 3-pyridyl-1*H*-pyrazole was selected as the N^N ligand owing to its exceptional structural versatility, enabling straightforward metal coordination in a chelating manner. This ligand offers the potential for lysosome targeting and incorporates a biologically friendly motif, thanks to the presence of the pyrazolyl unit, Fig. 2(A). Hence, the Ir^{III}-dimer was treated with 3-pyridyl-1*H*-pyrazole to obtain either a neutral complex **1**, if Cs_2CO_3 in DCM was used as an extrinsic base, or a cationic analogue **2** when no base and a mixture of DCM : MeOH (1 : 1) was utilised. In both cases purification step was undertaken by column chromatography, rendering the desired complexes **1** and **2** as orange solids in moderate yields of 82% and 76%, respectively (Fig. 2(C) and S3–S7†).

The structures of both complexes were corroborated using ^{1}H and $^{13}C\{^1H\}$ spectroscopy and assignation of the peaks was possible by means of two-dimensional (2D) NMR experiments (^{1}H-COSY, HSQC and HMBC). Coordination of the N^N ligand breaks the C_2-symmetry of the Ir-dimer, causing the two C^N ligands to become inequivalent and, in consequence, doubling the number of peaks for the C^N ligands. This resulted in distinct splitting patterns for each proton of the mpc ligand. Specifically, protons within the quinoline fragment experienced an upfield shift, while those within the phenyl fragment were slightly shifted downfield related to the initial Ir^{III}-dimer.[16] A comparison of the ^{1}H-NMR spectra of $[Ir(mpc)_2(\mu\text{-}Cl)]_2$ (Ir-dimer) and complex **1** and **2** are shown in Fig. 3(A), illustrating the asymmetric pattern and the chemical shifts upon coordination of 3-pyridyl-1*H*-pyrazole. The main difference between complexes **1** and **2** is the presence or absence of the NH proton at the pyrazole moiety. This difference is clearly shown in the ^{1}H-NMR spectra, where the broad peak integrating for one proton at 13.95 ppm in **2** is absent in **1**. Moreover, as result of the NH pyrazolyl deprotonation, pyrazole protons H(24) and H(25) shifted upfield from 6.98 and 7.86 ppm in **2** to 6.37 and 7.21 ppm in **1** respectively, which is consistent with similar complexes reported by Davis and coworkers.[17] Moreover, ^{13}C-NMR spectra followed the same trend displaying the asymmetric pattern for **1** and **2**, Fig. S4 and S7.† High resolution mass spectra showed the characteristic Ir isotope patterns for the neutral $[M + H]^+$ and cationic $[M]^+$ complex at *m*/*z* 862.1988 and 862.1979 respectively, Fig. S5 and S8.†

Photophysical study

Optical properties of **1** and **2** were investigated in DMSO solution at room temperature and the most relevant data is collected in Table 1. The UV-Visible spectra of **1** and **2** exhibited strong absorption bands below 300 nm, which can be assigned

Table 1 Photophysical data of **1** and **2** measured in DMSO solution at 298 K

	1	**2**
λ_{abs} [a] [nm] ($\varepsilon \times 10^4$/dm^3 mol^{-1} cm^{-1})	273 (9.1), 357 (4.2), 461 (1.1)	271 (6.9), 259 (6.0), 355 (3.3), 464 (0.6)
λ_{em} [a] [nm] (λ_{exc}, [nm])	720 (590)	690 (610)
ζ^a [ns]	50	265
Φ^a	19.7%	23.6%
Φ^b	41.6%	56.1%

[a] Aerated DMSO solution. [b] Deoxygenated DMSO solution.

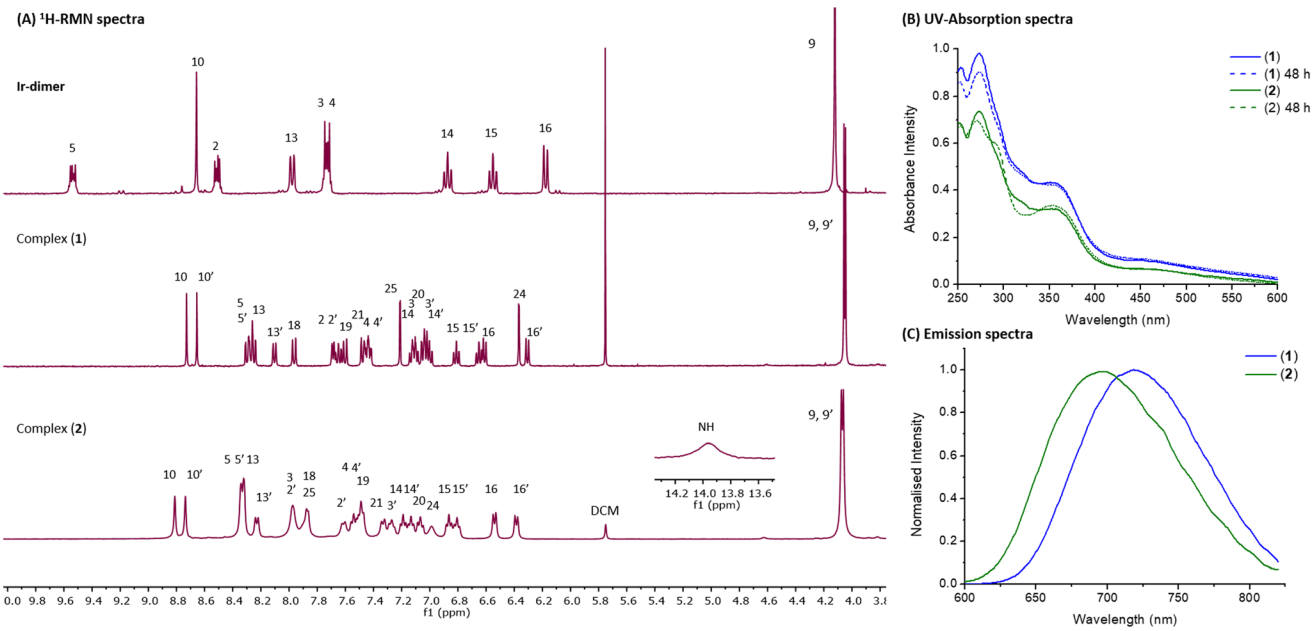

Fig. 3 (A) Staked ^{1}H-NMR (400 MHz) spectra of Ir-dimer and complexes **1** and **2** collected in d^6-DMSO at 298K. (B) UV-vis absorption spectra of **1** and **2** in DMSO at 298 K, and study of their stability in physiological conditions (310.5 K) after 48 h. (C) Normalised emission spectra of complexes **1** and **2** collected in aerated DMSO at r.t. upon excitation at 425 nm.

to ligand-centred spin-allowed (^{1}LC, $\pi \rightarrow \pi^*$) transitions, involving both, phenylquinoline and pyridylpyrazolyl derivates.[18] Both spectra also displayed weaker and broader bands between 320 and 400 nm. These bands, likely arising from charge transfer (CT) transitions, could be attributed to ^{1}MLCT and ^{1}LLCT transitions due to their structureless nature and smaller extinction coefficients.[19] Above 400 nm, a smaller band with a long tail reaching 600 nm is noticeable, which is typically associated with a forbidden ^{3}MLCT transition in this type of complex (Fig. 3(B)).[20] Stability of **1** and **2** in DMSO solution was also monitored by UV-Vis spectroscopy. The similarity of the UV-Vis absorption spectra profiles at 0 and 48 h revealed that these complexes are stable in those conditions, Fig. 3(B). Concerning their emission spectra, complexes **1** and **2** displayed structureless emission bands with maximum peaks at 720 nm and 690 nm, respectively, along with significant Stokes shifts, Fig. 3(C) and Table 1. These emission bands can be attributed to mainly ^{3}MLCT and ^{3}LLCT transitions. This assignment of origin is consistent with that reported for similar complexes in the literature.[21] Additionally, these data clearly showed that the charge of complexes influences the emission maximum promoting a shift from less energetic in neutral species (**1**) to more energetic emission in cationic species (**2**) as a consequence of changes in the energy of frontier orbitals. In this particular case, it can be proposed that protonation of the pyridylpyrazol renders less electron density on the Ir^{III} metal center, lowering the energy of the HOMO orbitals[22] and blue-shifting the emission maxima from 720 to 690 nm. Such behaviour was corroborated upon HCl addition to a DMSO solution of **1**, Fig. S10.† Notably, the 30 nm red shift is much greater than that observed for analogue complexes ($\Delta\lambda$ = 12 nm)[17] in cases where C^N ppy instead of mpc. This suggests that compounds **1** and **2** could be promising candidates for pH sensors. Accordingly, the smaller energy gap between the HOMO and LUMO levels in **1** is reflected in the measured emission lifetime values, which are shorter compared to **2** (50 ns *vs.* 265 ns, respectively). Similarly, the quantum yield exhibits the same trend with increasing energy gap, with **1** showing a lower quantum yield compared to **2** (19.7 *vs.* 23.6). Furthermore, in both cases, the quantum yield was observed to increase in the absence of oxygen, with values of 41.6% and 56.1% obtained for **1** and **2**, respectively, suggesting that molecular oxygen may act as a quencher.

Cytotoxicity and photocytotoxicity

The initial stage in the biological exploration of compounds **1** and **2** involved the assessment of *in vitro* bioactivity using MTT-reduction assays. A549, a human non-small cell lung cancer cell line, and 4T1-luc2, a cell line derived from the 4T1 mouse mammary carcinoma cell line which mimics stage IV human breast cancer, were treated with compounds **1** and **2** under various conditions to assess their potential as both, chemotherapeutic and photosensitiser agents (see Table 2 and Fig. S11–S13†).

In the case of A549 cells, the obtained IC_{50} values revealed that both complexes exhibit moderate cytotoxicity in absence of irradiation (IC_{50}(**1**) > 200 μM, IC_{50}(**2**): 67.2 ± 1.2 μM) upon 24 h incubation. However, upon exposure to 470 nm irradiation for ten minutes, their antiproliferative potential increased considerably, with photocytotoxic index (PI) greater than 85 and 38, respectively. Incubation time also played a crucial role in the assay. When incubated for 48 h, both complexes showed an increment of antiproliferative activity even without irradiation in A549 cells (IC_{50}(**1**): 22.2 ± 0.9 μM, IC_{50}(**2**): 58.0 ± 1.6 μM). However, their best IC_{50} values were achieved, once again, after photoactivation, resulting in IC_{50} values in the low micromolar range (IC_{50}(**1**): 0.86 ± 0.05 μM, IC_{50}(**2**): 0.93 ± 0.07 μM), suggesting their great performance as PSs. In terms of dealing with 4T1-luc2 cells, complex **1** shows moderate cytotoxicity at 21.4 ± 0.8 μM, while its analogue, complex **2**, exhibits higher activity with an IC_{50} value of 4.6 ± 0.4 μM. The antiproliferative properties of these complexes have a clear dependence on incubation time. At 48 hours of incubation, their IC_{50} values drop to the nanomolar range in both cases (IC_{50}(**1**): 0.22 ± 0.05 μM, IC_{50}(**2**): 0.27 ± 0.08 μM), and this trend continues at 72 hours (IC_{50}(**1**): 0.14 ± 0.09 μM, IC_{50}(**2**): 0.22 ± 0.03 μM). In contrast with the higher photocytotoxicity seen against A549, photoactivation of **1** and **2** did not showed any significant increment of their antiproliferative activity in 4T1-luc2. Hence, in this case, **1** and **2** are best proposed as chemotherapeutic drugs against 4T1-luc2. Furthermore, a closer look to the IC_{50} data for both complexes

Table 2 IC_{50} values (μM) of **1** and **2** incubated in A549 and 4T1-luc2 cells and lymphocytes in dark and under irradiation. Incubation times of 24, 48 or 72 h. Data were obtained from quadruplicates of three independent experiments and expressed as mean values ± standard deviation (SD)

		A549			4T1-luc2			Lymphocytes	
		DARK	Irrad.[a]	PI[b]	DARK	Irrad.[a]	PI[b]	DARK	Irrad.[a]
1	24 h	>200	2.3 ± 0.2	86.9	21.8 ± 0.8	19.6 ± 1.3	1.1	>100	>100
	48 h	22.2 ± 0.9	0.86 ± 0.05	25.8	0.22 ± 0.05	—	—	—	—
	72 h	—	—	—	0.14 ± 0.09	—	—	98.6 ± 0.17	83.6 ± 0.27
2	24 h	67.2 ± 1.2	1.7 ± 0.3	39.5	4.6 ± 0.4	2.1 ± 0.7	2.2	>100	>100
	48 h	58.0 ± 1.6	0.93 ± 0.07	62.4	0.27 ± 0.08	—	—	—	—
	72 h	—	—	—	0.22 ± 0.03	—	—	96.3 ± 0.28	81.9 ± 0.30

[a] Irradiation at 470 nm during 10 min, dose of 15.2 J cm^{-2}. [b] PI: photocytotoxic index: ratio between IC_{50} value in dark and IC_{50} value after irradiation, PI = IC_{50}(dark)/IC_{50}(irrad.). IC_{50}(cisplatin): 0.2 μM at 72 h in lymphocytes.[27]

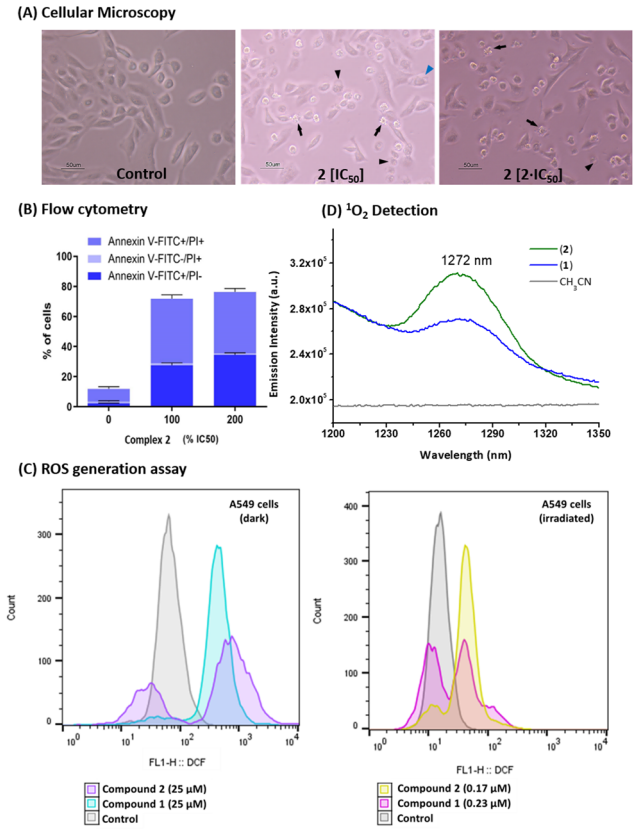

Fig. 4 (A) Cell microscopy images of **2** incubated with A549 for 24 h 470 nm (1.7 and 3.4 µM). Black arrows point to examples of apoptotic cells, blue triangles necrotic cells and black triangles point to possible parapoptotic cells. (B) Flow cytometry graph of **2** incubated with A549 for 24 h and irradiation at 470 nm during 10 min using Annexin V-FITC and PI as markers. (C) Flow cytometry graphs of ROS generation ability of **1** and **2** incubated with A549 cells for 24 h in dark and under irradiation (10 min, 470 nm, 15.2 J cm^{-2}) using DCFDA/H_2DCFDA as marker. (D) Emission of a solution of **1** (5×10^{-5} M CH_3CN, blue line), **2** (5×10^{-5} M CH_3CN red line) and neat CH_3CN (grey line).

indicated that their distinct nature (neutral *vs.* cationic) do not appear to significantly affect their *in vitro* antiproliferative potential. Therefore, it can be suggested that both of them behave similarly *in vitro*.

Recognising the exceptional multifunctionality of these complexes, which serve as both chemotherapeutic drugs and photosensitiser agents, prompted an investigation into the mechanisms of cell death in both conditions. Cellular bledding observed by optical microscopy is indicative of apoptotic cell death mechanism, Fig. 4(A) and S14.† To ascertain the cell death mechanism, flow cytometry analysis for complexes **1** and **2** was investigated upon incubation in dark and under irradiation in A549 cells. Annexin V-FITC and PI were used as markers for early (Annexin V-FITC satining) and late (dual Annexin V-FITC/PI staining).[23] The analysis clearly corroborated that both complexes induced cell death *via* an apoptotic pathway independent of both, concentration and incubation conditions, Fig. 4(B) and S15.† Additionally, the increased antiproliferative activity showed by **1** and **2** upon irradiation suggest that the generation of intracellular reactive oxygen species, ROS, might be implicated. Thus, ROS generation was investigated in A549 cells using flow cytometry. The assay revealed that both complexes generated ROS, not only under irradiation, but also in dark conditions, aligning with previous findings.[24] Histograms in Fig. 4(C) clearly showed the appearance of two peaks for each complex. The first peak can be associated with a population of dead cells, while the second peak corresponds to cells with a higher level of ROS generation. Among the ROS produced, it is likely that $^1O_2$ is generated, as previously reported for similar Ir^{III} complexes.[25] It is known that the phosphorescence of $^1O_2$ becomes evident *ca.* 1270 nm. Consequently, if $^1O_2$ is generated through irradiation, an emission band should be detected the by fluorescence spectroscopy.[26] Therefore, $^1O_2$ generation was addressed through steady-state fluorescence spectroscopy. Emission spectra of **1** and **2** were recorded upon excitation with a picosecond pulsed diode laser at 450 nm, revealing an emission band centered at 1272 nm, indicative of $^1O_2$ generation, Fig. 4(D). To rule out the possibility of an artefact from the spectrometer, an additional experiment was performed measuring a solution of acetonitrile (CH_3CN) in the absence of complexes. It can be concluded that both complexes induce $^1O_2$ production, which undoubtedly contributes to enhance the photocytotoxicity revealed *in vitro*.

The stability to light degradation of both complexes in the biological medium DMEN was investigated using absorption spectroscopy. In both cases, absorption bands were slightly modified compared to the initial spectra immediately after a cycle of irradiation. However, they regained their initial absorption pattern at 24 hours indicating their stability against light degradation, see Fig. S16.† Additionally, fluorescence spectroscopy assay was also performed to corroborate such stability to light degradation of the complexes. In both cases, it was observed an initial decrease in emission intensity upon irradiation at 470 nm for 10 minutes, which drop even lower after a second cycle of irradiation. However, emission intensity was significantly recovered after 24 h and remained similar at 48, suggesting once again the stability to light degradation even applying two cycles of irradiation. We speculate that the emission intensity drop seen just after applying the irradiation could be attributed to deactivation caused by $^1O_2$ formation.

Lymphocytes were then used as model for healthy cells to assess the cytotoxicity of **1** and **2** and comparison with that revealed in cancerous A549 and 4T1-luc2 cells. The MTT antiproliferative assays demonstrated that both complexes had no effect on lymphocytes after incubation for 24 or 72 hours, either in the dark or under irradiation conditions. In all cases, IC_{50} values were greater or close to 100 µM, see Table 2 and Fig. S13.† A flow cytometry assay revealed that both control and treated cells exhibited similar patterns, confirming that neither compound **1** nor compound **2** induces cell death in healthy cells, Fig. S17.† Therefore, cytotoxicity selectively arises against tumoral A549 and 4T1-luc2 cells.

The remarkable versatility of these complexes is evident, as they exhibit dual activity as both chemotherapeutic drugs and photosensitiser agents, contingent on the specific cell line being targeted for treatment. Moreover, no evident cytotoxicity was revealed for lymphocytes suggesting their higher selectivity towards tumoral A549 and 4T1-luc2 cells.

Intracellular organelle distribution

Fluorescence confocal microscopy assays were performed to investigate the intracellular organelle distribution of complex **2** in A549, see Fig. 5(A and B). Organelle-selective trackers CellTracker Blue (CTB) and LysoTracker Green (LTG) were used to ascertain the localization pattern through separate assessments. Subsequent irradiations at 405, 488 and 561 nm were used to visualise the emission from the CTB, LTG and complex **2** respectively. These assays demonstrated that the complex internalised into the A549 cells. However, when LTG was used as an internal standard, its fluorescence emission was absent upon irradiation at 488 nm, Fig. 5(A). Additionally, when the positive LTG control was conducted without the presence of **2**, it exhibited a vivid green emission (as shown in Fig. 5(C)) under identical irradiation conditions. This result implies that the presence of the complex could potentially suppress LTG's emission. This observation raises the possibility that both, compound **2** and LTG, might be situated within the same organelle for this suppression to occur. Given that LTG specifically targets lysosomes, it is highly likely that lysosomes are the organelles where complex **2** is predominantly located.

Fluorescence spectroscopy further confirmed the proposed quenching effect of **2** over LTG. Fig. 5(D) clearly showed that emission intensity of a solution of LTG at 525 nm was dismissed over time in the presence of complex **2**. After establishing that 20 minutes were sufficient for complex **2** to reduce the LTG emission intensity up to half, a slightly different fluorescence microscopy experiment was utilised to determine the distribution of **2** within 4T1-luc2 cells. This time LTG was added just prior to image collection. Confocal superimposed image in Fig. 5(E) demonstrated that complex **2** was also internalised in lysosomes in 4T1-luc2. Therefore, it can be concluded that complex **2** has a lysosomal localisation in both, A549 and 4T1-luc2. Lysosomal internalisation is often observed in Ir^{III} species containing ligands with protonable amine groups[13] as in the case of **1** and **2**. Additionally, given the structural similarity between both complexes, a comparable lysosomal distribution is expected for complex **1**.

In vivo assays

After validating the *in vitro* performance of **1** and **2**, and confirming their ability to inhibit the cell proliferation as chemotherapeutic drugs in the case of 4T1-luc2, a new study was designed to evaluate their toxicity and efficiency potential *in vivo*. In first place the toxicity of **1** and **2** was assessed using

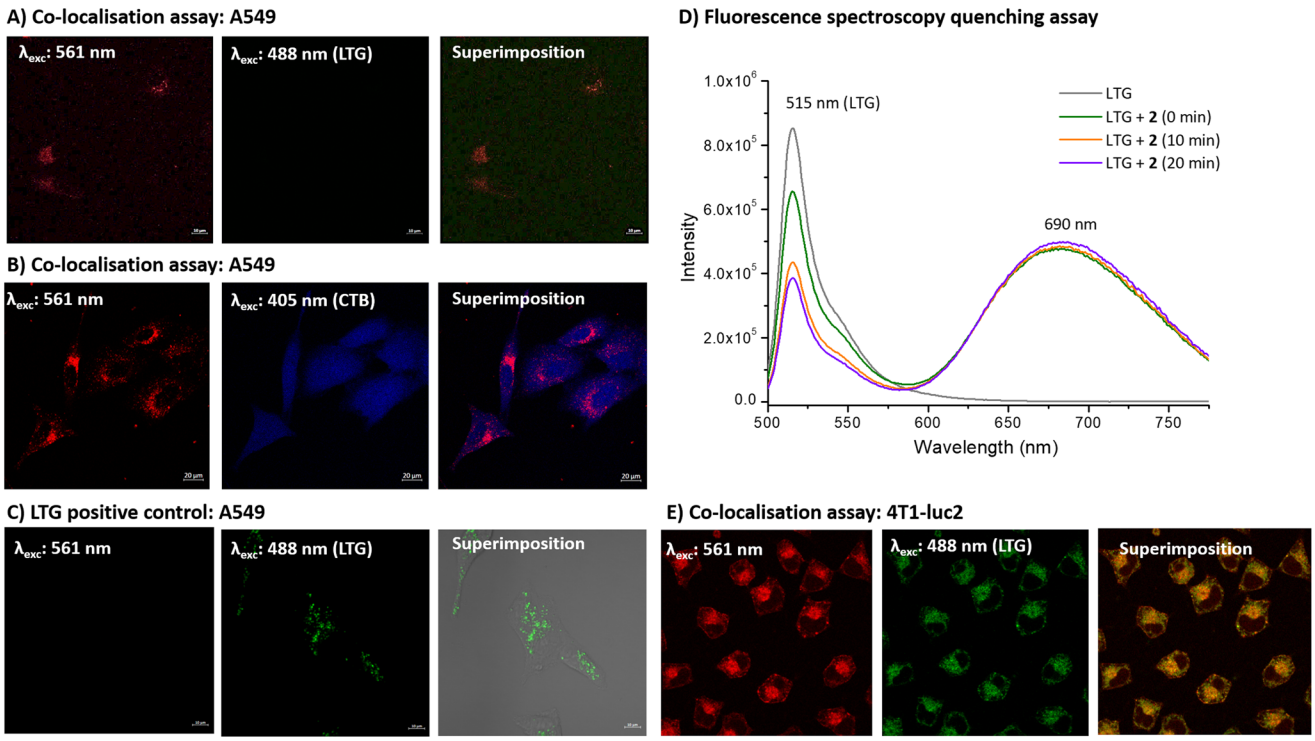

Fig. 5 (A and B) confocal microscopy images of A549 incubated with **2** (2 μM) for 2 hours, followed by the addition of organelle-selective trackers, LysoTracker Green (LTG, 45 min incubation, 100 nM) and CellTracker Blue (CTB, 30 min incubation, 500 mM). Excitation lasers at 405, 488 and 561 nm were employed for activate CTB, LTG and complex **2** respectively. Emission optical window was 407–480 nm for CTB, 500–560 nm for LTG and 575–715 nm for complex **2**. (C) Positive control: A549 and LTG. (D) Evolution of emission spectra of LTG in presence of complex **2**. (E) Confocal microscopy images of 4T1-luc2 incubated with **2** (2 μM) for 2 hours, followed by the addition of organelle-selective trackers, LysoTracker Green (LTG, 3–5 minutes incubation, 100 mM).

an acute oral toxicity test according to the OECD Test No. 425: Acute Oral Toxicity: Up-and-Down Procedure.[28] The starting dose of 17.5 mg kg^{-1} was administered to a group of 8 RjOrl: SWISS mice aged 10–11 weeks, at dosing intervals of 48 h. The highest dose tested was 175 mg kg^{-1}. The health of the animals was measured by weighing them and assessing their general status, spontaneous and provoked behaviour, using a modified evaluation scale to that established by Morton and Griffiths,[29] see Table S1.† These data were collected for a total of 14 days revealing no loss of animal welfare in any of the mice during experiment (Table S2†). In fact, the first 24 to 48 h after administration are critical for the toxicity to be detected, which would lead to a drastic decrease of the mice weight. Both compound showed less than 5% loss weight within those critical hours, see Table S3.† Likewise, within two week of the initial administration, there was even a slight increase in weight, comparable to the typical growth rate for the specific mice stain of that age. This demonstrates the absence of any toxic effects from complex **1** and **2** at the maxima administered dose, 175 mg kg^{-1} (Tables S2 and S3†).

Once it was observed that no toxic effects occurred, the next step was to evaluate their chemotherapeutic efficacy in the mammary carcinoma cell line 4T1-luc2. As commented previously 4T1 has been used in many research studies to mimic human breast cancer at stage IV.[30] In the particular case of in 4T1-luc2 cells, they have been genetically modified to express luciferase, a bioluminescent enzyme. As a consequence, this cell line is commonly used in preclinical studies to evaluate the efficacy of anticancer therapies in mouse models of breast cancer *via* non-invasive imaging.[31] Two distinct efficiency assays were developed to assess the effectiveness of potential therapeutics in early-stage (trial 1) and late-stage in vascularised and organised tumors (trial 2) (Fig. 6(A)).

In the trial 1, the progression of tumor growth was monitored using optical images that relied on bioluminescence (BLI) produced by the luciferin–luciferase system. This allowed us to track tumor growth even when it was not yet visible to the naked eye. 4T1-luc2 cells were subcutaneously implanted in 36 mice BALB/cByJRj strain. In the following day, optical imaging was performed to establish the four balanced experimental groups, negative control group (a), two treatment groups (b) and (c) and a positive control group treated with 5-fluorouracil a gold standard (d), a commonly used chemotherapeutic drug for treating breast cancer.[32] Mice in groups (b) and (c) were then orally treated with 1 mg kg^{-1} of the corresponding compounds **1** and **2**, respectively, as a suspension in a physiological saline buffer containing 5% DMSO. Mice in group (d) were also treated with 1 mg kg^{-1} of 5-fluorouracil, but this time it was administered *via* intraperitoneal injection, following the guidelines for the administration of this drug. It is worth noting that the typical administration of this drug is at 35 mg per kg of body weight. However, the dose was reduced in order to facilitate a fair comparison with complexes **1** and **2**.

This assay lasted for 11 days, with the optical imaging follow-up, mice weight measurements, and treatment administered on days 1, 5, 7, and 11, see Fig. 6(A). Representation of the bioluminescence emission intensity against the days elapsed clearly showed that **1** and **2** were able to significantly slowdown the proliferation of 4T1-luc2 cells at early stages. Fig. 6(B) (Table S4†) clearly illustrates a significant reduction in the emission intensity originating from the tumor area in mice treated with both complexes. This reduction is also evident in the lower tumor growth rates. In the early stages, it is reasonable to assume a growth rate constant independent of tumor size. Therefore, an exponential growth model can be applied following eqn (1) in Fig. 6(C), where BLI(t) represents the bioluminescence intensity as a function of time, $BLI_{(0)}$ is the bioluminescence intensity at $t = 0$, r is the growth rate constant, and t is the time elapsed. Mathematical transformation allowed the determinate the tumor growth rates of the different experimental groups. The control group (a) had a growth rate constant of 0.54 day^{-1} (in consonance with the literature, 0.57 day^{-1})[33] while group (b) and group (c) exhibited values of 0.30 day^{-1} and 0.46 day^{-1}, respectively, highlighting the reduced predisposition of tumors to grow following treatment, Fig. 6(D). Additionally, the similarity in the growth tumoral constant observed in mice groups treated with complexes **1** and **2** suggests that both compounds have a similar effectiveness in early tumoral stages, aligning with our *in vitro* observations.

For the second efficiency test in well-organised and vascularised tumors, trial 2, a measurement of tumor caliper was used instead of bioluminescence. In advanced stages, it is more accurate to measure the size and volume of tumors using a caliper rather than relying on the bioluminescence emitted by larger tumors, which may be in a necrotic stage and therefore emit an uneven signal. Thus, tumor cells were subcutaneously injected into 21 mice (BALB/cByJRj) on day 0, but this time the mice were not treated until day 14. On that day, the mice were divided into two balanced groups: a negative control group (a′) and a treatment group (b′), that were treated in this case with complex **1**, seen the similar effectiveness at early tumoral stages with complex **2**. Administration, tumoral volume and mice weight measurements were performed on days 14, 18, 21, 25 and 32, as depicted in Fig. 6(A). Fig. 6(E) presents the tumoral volume for both groups (a′ and b′) from day 14 until day 32. A noticeable decrease in tumor size became evident after day 21, see Table S5.† This reduction was statistically validated by Mann–Whitney test, indicating a significant decline in tumor growth from this point onward in the treated group. On day 32, the data clearly illustrates that administering complex **1** to the mice (group b′) resulted in a substantial reduction in tumor size, decreasing its volume by nearly half. Importantly, no significant differences in the mice's weight were observed in both group 'a' and group 'b', indicating that repeated dose administration did not result in any toxicity. However, concerning tumor ulceration, on day 32, 8 out of 10 mice in the control group exhibited ulcerated tumors, whereas only 4 out of 11 mice in the treated group did, suggesting slower tumor growth in the treated group following treatment with compound **1**. Consequently, on day 32,

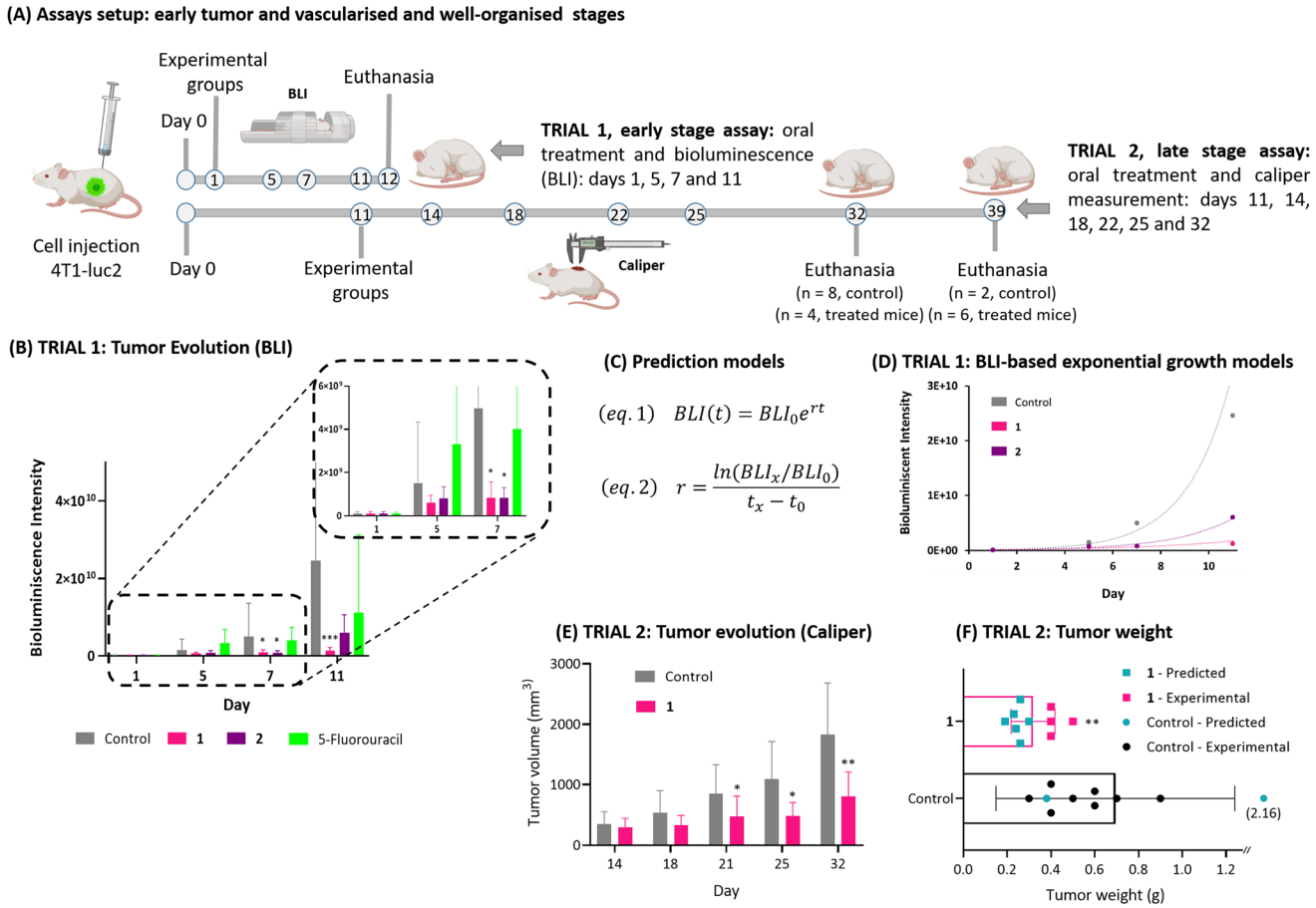

Fig. 6 (A) Followed setup for evaluation of **1** and **2** and fluorouracil *in vivo* at early tumoral stages (trial 1) and complex **1** in vascularised and well organised 4T1-luc2 tumors (trial 2). The administration route was oral for **1** and **2** at 1 mg kg^{-1} and intraperitoneal injection for fluorouracil at 1 mg kg^{-1}. (B) Tumoral evolution recorded by bioluminescence (BLI), control group (grey bar), mice treated **1** (pink bar) with **2** (purple bar) and 5-fluorouracil (green bar) at days 1, 5, 7 and 11. Data are presented as mean ± SD, n = 9 (**1**), n = 9 (**2**), n = 9 control $^*P < 0.05$, $^{***}P < 0.001$ indicates comparison with the control group. (C) Tumor growth prediction models for BLI. (D) BLI-based exponential growth models for control group, **1** and **2**. (E) Volume of the tumor measured by caliper measured on days 14, 18, 25 and 32 of mice in the control group mice treated oraly with **1** (1 mg kg^{-1}). Data are presented as mean ± SD, n = 11 (**1**), n = 10 (control), $^{**}P < 0.01$ and $^{***}P < 0.001$ indicates comparison with the control group. (F) Predicted and experimental tumor weight of isolated tumors at day 32 removed upon euthanasia. Data are presented as mean ± SD, n = 11 (**1**), n = 10 (control), $^{**}P < 0.01$ indicates comparison with the control group.

the mice with ulcerated tumors were euthanized as a humane endpoint (HEP). The remaining mice were monitored until day 39, at which point the trial was terminated. See Table S6† for details. Tumor weight was then recorded upon isolation on both euthanasia days, as shown in Fig. S18.† It is well-known that caliper measurements and tumor weight are correlated variables (both dependent on the cancer cell count).[34] Consequently, a tumor growth model was developed using the caliper data, eqn (S1) and (S2).† This model quantifies and predicts the tumoral weight for each animal on a specific day of the experiment. Therefore, we were able to estimate the tumor weight on day 32 for the mice treated and euthanised on day 39 (Fig. 6(F) and S19†). A significant reduction in tumor weight was observed in mice treated with compound **1** compared to the control group, with weights of 0.31 ± 0.03 g and 0.69 ± 0.17 g, respectively. Moreover considering difference between the incidence of tumor ulceration among the control and treated mice, it becomes evident that the administration of complexes **1** significantly impedes tumor growth even in the later stages of tumor progression. In summary, these findings underscore the potential of complex **1** as highly promising candidate for chemotherapy targeting 4T1-luc2 tumors at both early and advanced stages. This provides a strong foundation for continued research into this class of cyclometallated iridium compounds.

Conclusions

In conclusion, our research has resulted in the development of luminescent neutral complex **1** and cationic complex **2**, both cyclometallated Ir^{III} complexes with pyrazolyl derived ligands designed as versatile and readily synthesisable anticancer agents with a lysosomal targeting strategy. These compounds

exhibit dual functionality, serving as effective chemotherapeutic agents and photosensitisers, with their optimal performance contingent upon the specific cancer cell line. A549 cells demonstrated heightened sensitivity to phototherapeutic treatment with **1** and **2**, while 4T1-luc2 cells exhibited superior responses to chemotherapeutic approaches. Significantly, these complexes displayed selective activity against cancer cells, leaving healthy cells unharmed.

Flow cytometry investigations indicated an apoptotic cell death mechanism and ROS generation for both therapeutic approaches, and fluorescence NIR spectroscopy highlighted singlet oxygen ($^1O_2$) as a key cytotoxic agent in the phototherapeutic approach. *In vivo* studies revealed minimal toxicity and remarkable effectiveness against 4T1-luc2 cells, surpassing the performance of clinically employed drugs at early tumor stages and even at vascularised and organised tumor stages. While further investigations are warranted, these findings strongly suggest the potential of these pyrazolyl-based Ir^{III} complexes for the treatment of breast cancer. Their adaptability to target specific cancer cell lines, either as chemosensitisers for photodynamic therapy (PDT) or as chemotherapeutics, combined with their ease of synthesis, positions them as promising candidates for future research, paving the way for innovative approaches in cancer therapy.

Data availability

The data that support the findings of this study are available in the ESI,† which includes general measurement conditions, analysis instrumentation, experimental procedures and characterisation, photophysical studies and *in vitro* and *in vivo* assays.

Author contributions

Conceptualization, M.C.G. and V.F.-M.; synthesis of the probes, M.R.; evaluation of the photophysical properties, M.R. and V.F.-M.; evaluation of the bioactive properties *in vitro*, M. R., A.B. and I.M.; evaluation of the bioactive properties *in vivo*, E.R.; non-parametrical statistical study: G.C.B.; data curation, V.F.-M. and M.R.; writing—original draft preparation, V.F.-M. and M.R.; writing—review and editing, V.F.-M., M.C.G., M.R., A.B., G.C.B. and E.R.; Supervision, V.F.-M. and M.C.G.; project administration, V.F.-M. and M.C.G.; funding acquisition, V. F.-M. and M.C.G. All authors have read and agreed to the published version of the manuscript.

Conflicts of interest

There are no conflicts of interest to declare.

Acknowledgements

Authors thank the Agencia Estatal de Investigación PID2022-136861NB-I00/AEI/10.13039/501100011033; PID2022-137862NB-I00/AEI/10.13039/501100011033, and Gobierno de Aragón-Fondo Social Europeo (E07_23R) for financial support. M. R. and A. B. thanks the Gobierno de Aragón for a predoctoral fellowship.

References

1 (*a*) V. Venkatesh, R. Berrocal-Martin, C. J. Wedge, I. Romero-Canelon, C. Sanchez-Cano, J.-I. Song, J. P. C. Coverdale, P. Zhang, G. J. Clarkson, A. Habtemariam, S. W. Magennis, R. J. Deeth and P. J. Sadler, Mitochondria-targeted spin-labelled luminescent iridium anticancer complexes, *Chem. Sci.*, 2017, **8**, 8271–8278; (*b*) J. Yang, H.-J. Fang, Q. Cao and Z.-W. Mao, The design of cyclometalated iridium(III)–metformin complexes for hypoxic cancer treatment, *Chem. Commun.*, 2021, **57**, 1093–1096; (*c*) G. Millán, M. Nieddu, I. P. López, C. Ezquerro, J. R. Berenguer, I. M. Larráyoz, J. G. Pichel and E. Lalinde, A new family of luminescent iridium complexes: synthesis, optical, and cytotoxic studies, *Dalton Trans.*, 2023, **52**, 6360–6374; (*d*) M. Redrado, A. Benedi, I. Marzo, A. L. García-Otín, V. Fernández-Moreira and M. C. Gimeno, Multifunctional heterometallic IrIII–AuI probes as promising anticancer and antiangiogenic agents, *Chem. – Eur. J.*, 2021, **27**, 9885–9897.

2 (*a*) R. Bevernaegie, B. Doix, E. Bastien, A. Diman, A. Decottignies, O. Feron and B. Elias, Exploring the phototoxicity of hypoxic active iridium(III)-based sensitizers in 3D tumor spheroids, *J. Am. Chem. Soc.*, 2019, **141**, 18486–18491; (*b*) L. Wang, J. Karges, F. Wei, L. Xie, Z. Chen, G. Gasser, L. Jia and H. Chao, A mitochondria-localized iridium(III) photosensitizer for two-photon photodynamic immunotherapy against melanoma, *Chem. Sci.*, 2023, **14**, 1461–1471; (*c*) X. He, L. Wei, J. Chen, S. Ge, M. Kandawa-Shultz, G. Shao and Y. Wang, Folate-targeted iridium complexes amplify photodynamic therapy efficacy through ferroptosis, *Inorg. Chem. Front.*, 2023, **10**, 4780–4788.

3 (*a*) A. Luengo, I. Marzo, M. Reback, I. M. Daubit, V. Fernández-Moreira, N. Metzler-Nolte and M. C. Gimeno, Luminescent bimetallic IrIII/AuI peptide bioconjugates as potential theranostic agents, *Chem. – Eur. J.*, 2020, **26**, 12158–12167; (*b*) J. Li, H. Chen, L. Zeng, T. W. Rees, K. Xiong, Y. Chen, L. Ji and H. Chao, Mitochondria-targeting cyclometalated iridium(III) complexes for tumor hypoxic imaging and therapy, *Inorg. Chem. Front.*, 2019, **6**, 1003–1010; (*c*) M. Redrado, V. Fernández-Moreira and M. C. Gimeno, Theranostics through the synergistic cooperation of heterometallic complexes, *ChemMedChem*, 2021, **16**, 932–941.

4 (*a*) S. Yoon and T. S. Teets, Enhanced deep red to near-infrared (DR-NIR) phosphorescence in cyclometalated

iridium(III) complexes, *Inorg. Chem. Front.*, 2022, **9**, 6544–6553; (*b*) C. Wu, K.-J. Wu, J.-B. Liu, W. Wang, C.-H. Leung and D.-L. Ma, Structure-guided discovery of a luminescent theranostic toolkit for living cancer cells and the imaging behavior effect, *Chem. Sci.*, 2020, **11**, 11404–11412.

5 M. J. Naim, O. Alam, F. Nawaz, M. J. Alam and P. Alam, Current status of pyrazole and its biological activities, *J. Pharm. BioAllied Sci.*, 2016, **8**, 2–17.

6 (*a*) P. R. Wyde, B. E. Gilbert and M. W. Ambrose, Comparison of the anti-respiratory syncytial virus activity and toxicity of papaverine hydrochloride and pyrazofurin in vitro and in vivo, *Antiviral Res.*, 1989, **11**, 15–26; (*b*) G. J. Kapadia, H. Tokuda, R. Sridhar, V. Balasubramanian, J. Takayasu, P. Bu, F. Enjo, M. Takasaki, T. Konoshima and H. Nishino, Cancer chemopreventive activity of synthetic colorants used in foods, pharmaceuticals and cosmetic preparations, *Cancer Lett.*, 1998, **129**, 87–95; (*c*) A. A. Abbas, M. H. Abdellattif and K. M. Dawood, Inhibitory activities of bipyrazoles: a patent review, *Expert Opin. Ther. Pat.*, 2022, **32**, 63–87.

7 (*a*) G. Friedrich, T. Rose and K. Rissler, Determination of lonazolac and its hydroxy and O-sulfated metabolites by on-line sample preparation liquid chromatography with fluorescence detection, *J. Chromatogr. B: Anal. Technol. Biomed. Life Sci.*, 2002, **786**, 295–305; (*b*) J. Pantel, S. Y. Williams, D. Mi, J. Sebag, J. D. Corbin, C. D. Weaver and R. D. Cone, Development of a high throughput screen for allosteric modulators of melanocortin-4 receptor signaling using a real time cAMP assay, *Eur. J. Pharmacol.*, 2011, **660**, 139–147; (*c*) G. S. Hassan, S. M. Abou-Seri, G. Kamel and M. M. Ali, Celecoxib analogs bearing benzofuran moiety as cyclooxygenase-2 inhibitors: Design, synthesis and evaluation as potential anti-inflammatory agents, *Eur. J. Med. Chem.*, 2014, **76**, 482–483; (*d*) M. Giorgi, G. Mengozzi, A. Rafaelli and A. Saba, Characterization of in vivo plasma metabolites of tepoxalin in horses using LC-MS-MS, *J. Pharm. Biomed. Anal.*, 2011, **56**, 45–53; (*e*) G. Dowling and E. Malone, Analytical strategy for the confirmatory analysis of the non-steroidal anti-inflammatory drugs firocoxib, propyphenazone, ramifenazone and piroxicam in bovine plasma by liquid chromatography tandem mass spectrometry, *J. Pharm. Biomed. Anal.*, 2011, **56**, 359–365.

8 (*a*) T. Kameyama and T. Nabeshima, Effects of 1,3-diphenyl-5-(2-dimethylaminopropionamide)-pyrazole[difenamizole] on a conditioned avoidance response, *Neuropharmacology*, 1978, **17**, 249–256; (*b*) Z.-H. Song and N. Zhang, In vitro detecting ultra-trace novalgin in medicine and human urine by chemiluminescence, *Talanta*, 2003, **60**, 161–170.

9 J. Yellol, S. A. Pérez, G. Yellol, J. Zajac, A. Donaire, G. Vigueras, V. Novohradsky, C. Janiak, V. Brabec and J. Ruiz, Highly potent extranuclear-targeted luminescent iridium(III) antitumor agents containing benzimidazole-based ligands with a handle for functionalization, *Chem. Commun.*, 2016, **52**, 14165–14168.

10 (*a*) N. Wu, J.-J. Cao, X.-W. Wu, C.-P. Tan, L.-N. Ji and Z.-W. Mao, Iridium(III) complexes with five-membered heterocyclic ligands for combined photodynamic therapy and photoactivated chemotherapy, *Dalton Trans.*, 2017, **46**, 13482–13491; (*b*) R. P. Paitandi, S. Mukhopadhyay, R. S. Singh, V. Sharma, S. M. Mobin and D. S. Pandey, Anticancer activity of iridium(III) complexes based on a pyrazole-appended quinoline-based BODIPY, *Inorg. Chem.*, 2017, **56**, 12232–12247.

11 (*a*) C.-W. Hsu, E. Longhi, S. Sinn, C. S. Hawes, D. C. Young, P. E. Kruger and L. De Cola, Pyrazolo[4,3 h]quinoline ligand-based iridium(III) complexes for electrochemiluminescence, *Chem. – Asian J.*, 2017, **12**, 1649–1658; (*b*) C. Li, G. Zhang, H.-H. Shih, X. Jiang, P. Sun, Yi Pan and C.-H. Cheng, High-efficient phosphorescent iridium(III) complexes with benzimidazole ligand for organic light-emitting diodes: Synthesis, electrochemistry and electroluminescent properties, *J. Organomet. Chem.*, 2009, **694**, 2415–2420; (*c*) J. Zheng, W. B. Swords, H. Jung, K. L. Skubi, J. B. Kidd, G. J. Meyer, M.-H. Baik and T. P. Yoon, Enantioselective intermolecular excited-state photoreactions using a chiral Ir triplet sensitizer: separating association from energy transfer in asymmetric photocatalysis, *J. Am. Chem. Soc.*, 2019, **141**, 13625–13634.

12 (*a*) P. Saftig and K. Sandhoff, Killing from the inside, *Nature*, 2013, **502**, 312–313; (*b*) T. Tang, Z.-Y. Yang, D. Wang, X.-Y. Yang, J. Wang, L. Li, Q. Wen, L. Gao, X.-W. Bian and S.-C. Yu, The role of lysosomes in cancer development and progression, *Cell Biosci.*, 2020, **10**, 131–145.

13 (*a*) L. He, Y. Li, C.-P. Tan, R.-R. Ye, M.-H. Chen, J.-J. Cao, L.-N. Jia and Z.-W. Mao, Cyclometalated iridium(III) complexes as lysosome-targeted photodynamic anticancer and real-time tracking agents, *Chem. Sci.*, 2015, **6**, 5409–5418; (*b*) F.-X. Wang, M.-H. Chen, Y.-N. Lin, H. Zhang, C.-P. Tan, L.-N. Ji and Z.-W. Mao, Dual functions of cyclometalated iridium(III) complexes: anti-metastasis and lysosome-damaged photodynamic therapy, *Appl. Mater. Interfaces*, 2017, **9**(49), 42471–42481.

14 S. DasGupta, P. R. Murumkar, R. Giridhar and M. R. Yadav, Studies on novel 2-imidazolidinones and tetrahydropyrimidin-2(1 h)-ones as potential TACE inhibitors: design, synthesis, molecular modeling, and preliminary biological evaluation, *Bioorg. Med. Chem.*, 2009, **17**, 3604–3617.

15 S. Lamansky, P. Djurovich, D. Murphy, F. Abdel-Razzaq, H.-E. Lee, C. Adachi, P. E. Burrows, S. R. Forrest and M. E. Thompson, Highly phosphorescent bis-cyclometalated iridium complexes: synthesis, photophysical characterization, and use in organic light emitting diodes, *J. Am. Chem. Soc.*, 2001, **123**, 4304–4312.

16 J.-H. Zhu, G.-X. Xu, J. Shum, L. C.-C. Lee and K. K.-W. Lo, Tuning the organelle specificity and cytotoxicity of iridium (III) photosensitisers for enhanced phototheranostic applications, *Chem. Commun.*, 2021, **57**, 12008–12011.

17 N. S. Y. Abdolla, D. L. Davies, M. P. Lowe and K. Singh, Bis-cyclometallated Ir(iii) complexes containing 2-(1H-pyrazol-

3-yl)pyridine ligands; influence of substituents and cyclometallating ligands on response to changes in pH, *Dalton Trans.*, 2020, **49**, 12025–12036.

18 F. Lafolet, S. Welter, Z. Popović and L. De Cola, Iridium complexes containing p-phenylene units. The influence of the conjugation on the excited state properties, *J. Mater. Chem.*, 2005, **15**, 2820–2828.

19 B. Liu, L. Lystrom, C. G. Cameron, S. Kilina, S. A. McFarland and W. Sun, Monocationic iridium(III) complexes with far-red charge-transfer absorption and near-IR emission: synthesis, photophysics, and reverse saturable absorption, *Eur. J. Inorg. Chem.*, 2019, **16**, 2208–2215.

20 L.-Q. Wei and B.-H. Ye, Cyclometalated Ir–Zr metal–organic frameworks as recyclable visible-light photocatalysts for sulfide oxidation into sulfoxide in water, *ACS Appl. Mater. Interfaces*, 2019, **11**, 41448–41457.

21 (*a*) J. R. Shakirova, O. A. Tomashenko, E. E. Galenko, A. F. Khlebnikov, P. Hirva, G. L. Starova, S.-H. Su, P.-T. Chou and S. P. Tunik, Metalated Ir(III) Complexes Based on the Luminescent Diimine Ligands: Synthesis and Photophysical Study, *Inorg. Chem.*, 2018, **57**, 6853–6864; (*b*) C. E. Elgar, H. Y. Otaif, J. M. Beames, P. N. Horton, S. J. Coles, A. J. Hallett, S. P. O'Kell and S. J. A. Pope, Deep red emitting heteroleptic Ir(III) complexes that incorporate unsymmetrical 4-quinoline carboxylic acid derived ligands, *Eur. J. Inorg. Chem.*, 2023, **26**, e20230012.

22 A. Luengo, M. Redrado, I. Marzo, V. Fernández-Moreira and M. C. Gimeno, Luminescent Re(I)/Au(I) species as selective anticancer agents for hela cells, *Inorg. Chem.*, 2020, **59**, 8960–8970.

23 M. van Engeland, L. J. Nieland, F. C. Ramaekers, B. Schutte and C. P. Reutelingsperger, Annexin V-affinity assay: a review on an apoptosis detection system based on phosphatidylserine exposure, *Cytometry*, 1998, **31**, 1–9.

24 L. Wang, J. Karges, F. Wei, L. Xie, Z. Chen, G. Gasser, L. Ji and H. Chao, A mitochondria-localized iridium(III) photosensitizer for two photon photodynamic immunotherapy against melanoma, *Chem. Sci.*, 2023, **14**, 1461–1471.

25 M. Redrado, M. Miñana, M. P. Coogan, M. C. Gimeno and V. Fernández-Moreira, Tunable emissive Ir(III) benzimidazole-quinoline hybrids as promising theranostic lead compounds, *ChemMedChem*, 2022, **17**, e202200244.

26 A. A. Gorman and M. A. J. Rodgers, New trends in photobiology: Current perspectives of singlet oxygen detection in biological environments, *J. Photochem. Photobiol., B*, 1992, **14**, 159–176.

27 (*a*) M. Fabijanska, M. M. Kasprzak and J. Ochocki, Ruthenium(II) and platinum(II) complexes with biologically active aminoflavone ligands exhibit in vitro anticancer activity, *Int. J. Mol. Sci.*, 2021, **22**, 7568; (*b*) M. Kasprzak, M. Fabijanska, L. Checinska, K. Studzian, M. Markowicz-Piasecka, J. Sikora and E. Mikiciuk-Olasik, Small differences in structure, a large difference in activity – Comparing a new Ru(II)-3-hydroxyiminoflavanone complex with analogous Ru(II) compounds J. Ochocki, *Inorg. Chim. Acta*, 2017, **457**, 69–80.

28 OECD, *Test No. 425: Acute Oral Toxicity: Up-and-Down Procedure*, OECD Guidelines for the Testing of Chemicals, Section 4, OECD Publishing, Paris, 2022, DOI: **10.1787/9789264071049-en**.

29 D. B. Morton and P. H. Griffiths, Guidelines on the recognition of pain, distress and discomfort in experimental animals and an hypothesis for assessment, *Vet. Rec.*, 1985, **116**, 431–436.

30 (*a*) J. Wang, R. Ocadiz-Ruiz, M. S. Hall, G. G. Bushnell, S. M. Orbach, J. T. Decker, R. M. Raghani, Y. Zhang, A. H. Morris, J. S. Jeruss and L. D. Shea, A synthetic metastatic niche reveals antitumor neutrophils drive breast cancer metastatic dormancy in the lungs, *Nat. Commun.*, 2023, **14**, 4790–4810; (*b*) S. S. Rao, G. G. Bushnell, S. M. Azarin, G. Spicer, B. A. Aguado, J. R. Stoehr, E. J. Jiang, V. Backman, L. D. Shea and J. S. Jeruss, Enhanced survival with implantable scaffolds that capture metastatic breast cancer cells in vivo, *Cancer Res.*, 2016, **76**, 5209–5218.

31 (*a*) J. B. Kim, K. Urban, E. Cochran, S. Lee, A. Ang, B. Rice, A. Bata, K. Campbell, R. Coffee, A. Gorodinsky, Z. Lu, H. Zhou, T. K. Kishimoto and P. Lassota, Non-invasive detection of a small number of bioluminescent cancer cells in vivo, *PLoS One*, 2010, **5**, e9364; (*b*) E. Katsuta, S. C. DeMasi, K. P. Terracina, S. Spiegel, G. Q. Phan, H. D. Bear and K. Takabe, Modified breast cancer model for preclinical immunotherapy studies, *J. Surg. Res.*, 2016, **204**, 467–474.

32 D. B. Longley, D. P. Harkin and P. G. Johnston, 5-fluorouracil: mechanisms of action and clinical strategies, *Nat. Rev. Cancer*, 2003, **5**, 330–336.

33 R. V. Simões, I. S. Serganova, N. Kruchevsky, A. Leftin, A. A. Shestov, H. T. Thaler, G. Sukenick, J. W. Locasale, R. G. Blasberg, J. A. Koutcher and E. Ackerstaff, Metabolic plasticity of metastatic breast cancer cells: adaptation to changes in the microenvironment, *Neoplasia*, 2015, **17**, 671–684.

34 (*a*) D. M. Euhus, C. Hudd, M. C. LaRegina and F. E. Johnson, Tumor measurement in the nude mouse, *J. Surg. Oncol.*, 1986, **31**, 229–234; (*b*) M. M. Tomayko and C. P. Reynolds, Determination of subcutaneous tumor size in athymic (nude) mice, *Cancer Chemother. Pharmacol.*, 1989, **24**, 148–154.

